Measurement of Elastic Microfence Deflection for Aerodynamic Flow Sensing

Aditya Saini[1], Taeyang Kim[1], Zheng Cui[1], Benjamin Schuessler[4], Frank L. Palmieri[2], John W. Connell[2], Yi Lin[3], Xiaoning Jiang[1], Yong Zhu[1], Ashok Gopalarathnam[1], Christopher J. Wohl[2]

1 Department of Mechanical and Aerospace Engineering, North Carolina State University, Raleigh, NC 27695, US
2 NASA Langley Research Center, Hampton, VA 23681, US
3 National Institute of Aerospace, Hampton, VA 23681, US
4 NIFS intern, NASA Langley Research Center, Hampton, VA 23681, US

E-mail: asaini2@ncsu.edu

October 2017

Abstract. Bio-inspired artificial hair sensors have the potential to detect aerodynamic flow features such as stagnation point, flow separation, and flow reattachment that could be beneficial for flight control and performance enhancement of aircraft. In this work, elastic microfence structures were tested on a flat-plate setup. The microfences were fabricated from a two-part silicone molded against a template patterned by laser ablation. The response of the microfences to different freestream velocities and to flow reversal at the sensor were recorded via an optical microscope.

Keywords: microfence, aerodynamics, wind tunnel, image processing, flow reversal

1. Introduction

Inspired by sensory structures in animals as diverse as bats [1], fishes [2], and insects [3], artificial hair sensors for aerodynamic flow sensing have gained much interest over the past few years. It is believed that birds and insects use various mechanoreceptors embedded in their wings to sense crucial information such as the flow speed, flow stagnation point, stall, and turbulence over the wing [1] and fine tune their flight performance [4, 5]. Birds can sense the slightest changes in the airflow; this enables them to stabilize in varying wind gusts and changing weather [6, 7]. Bats have the remarkable ability to reverse flight directions at high speeds in short distances [8].

For flight systems, the knowledge of the incoming aerodynamic flow can be useful for stall sensing, envelope protection and control. The mechanical response of microstructures can potentially be used for surface-flow sensing, especially in micro-air vehicles (MAVs) where conventional sensors demand too much power and space. Artificial microstructures immersed in the boundary layer can effectively respond to the changes in the boundary layer, identifying critical aerodynamic flow features such as stagnation point, laminar separation, and flow reattachment.

Micropillars can also provide a means of quantifying shear stress, if the height of the micropillar is restricted to stay within the viscous sublayer. The velocity profile can be assumed to be linear within the viscous sublayer of the boundary layer, making the pillar tip deflection indirectly correlate to the wall shear stress [9]. An array of cylindrical micropillars could provide complete spatial and temporal resolution of the shear stress [10, 11, 12, 13, 14, 15], making it a convenient and inexpensive alternative to conventional indirect shear stress measuring techniques, such as hot wire/film, oil interferometry, laser doppler velocimetry, or particle image velocimetry [16].

Smart materials systems such as carbon nanotube arrays [17, 18, 19] and piezeoelectric microstructures [20, 21, 22] can directly convert pillar deflection to electrical output. More complicated sensor designs and transduction mechanisms involve cylindrical microstructures attached to flexible platforms, where the rotational moment of the base of the pillar displaces the membrane underneath resulting in an electrical response in the form of capacitance, inductance or resistance change [23, 24, 25]. The moments at the bases of 1-mm cylindrical micropillars have been modeled to assess the ability of such pillars to detect boundary layer changes [2, 26].

This paper presents the experimental response of elastic surface topographies using optical measurement to track tip deflections. Most previous studies involving characterization of flow properties using elastic topographies have been conducted for pipe/duct flows or wall jet flows. In this study, fence-type microstructures were considered instead of micropillars for greater mechanical robustness, making them easier to fabricate. The responses of elastic microfence structures mounted on a flat plate in a subsonic wind tunnel were recorded via optical microscopy. Image stabilization algorithms along with integrated stationary fiducial-mark topographies were utilized to compensate for wind tunnel vibrations.

2. Sensor Fabrication and Transduction

Elastic surface topographies designed to be responsive to profile drag within the viscous sublayer, comprise the microfence structures. Templates (molds) were generated by patterning epoxy (Dow Chemical DER 331 : Ethacure 100, 1 : 0.8) substrates using laser ablation, enabling rapid design changes. Silicone material was cast on the template to generate the sensor surface. The technique allowed for good control of the depths of the pattern features. The sensing elements consisted of microfences with an aspect ratio of at least 3:1 (height:width). Microfences can be placed at various orientations relative to the freestream flow vector to determine shear stresses in different directions relative to the airflow. Stationary features (fiducial marks, long lines or dots that should not move in the airflow) were provided to enable position referencing (Figure 1). Featureless regions were included to prevent disruption of the airflow by upstream sensing elements. The fabrication process was described in more detail in Cisotto et al. [27], and some relevant design parameters are outlined in Table 1. The deflection of the elastic microfence structures due to the local flow condition was recorded using optical microscopy.

Table 1: Microfence design parameters.

Microfence features	Silicone	EcoFlex 00-10
	Height (μm)	80 - 100
	Aspect ratio	3
Laser parameters	Power (mW)	300 - 1000
	Pulse frequency (kHz)	80
	Mark speed (cm/s)	2.5
	Jump speed (cm/s)	10.2

Since the intention was to minimize disruption of the airflow by keeping the structures within the viscous sublayer, feature heights on the order of 50-100 μm were targeted. An optical microscope was constructed with emphasis placed on minimizing the interactions of the device with the airflow enabling ready implementation into the designed wind-tunnel model. The resultant instrument was approximately 20.32 cm $\times$ 20.32 cm $\times$ 25.4 cm (length $\times$ width $\times$ height) and consisted of a 10$\times$ microscope objective, with a long working distance, connected to an in-line light source and a charge-coupled device (CCD) camera. Since the current work aims at detecting surface-flow features, rather than accurate shear-stress measurement, the decision was made to use an inexpensive camera rather than one with a higher frame rate used in earlier works [10, 11, 13, 15]. The camera used was a progressive-scan CCD with a resolution of 1.3 Mp and frame rate of 15 fps. Success with such a lower-cost camera would more easily transition into real-world applications.

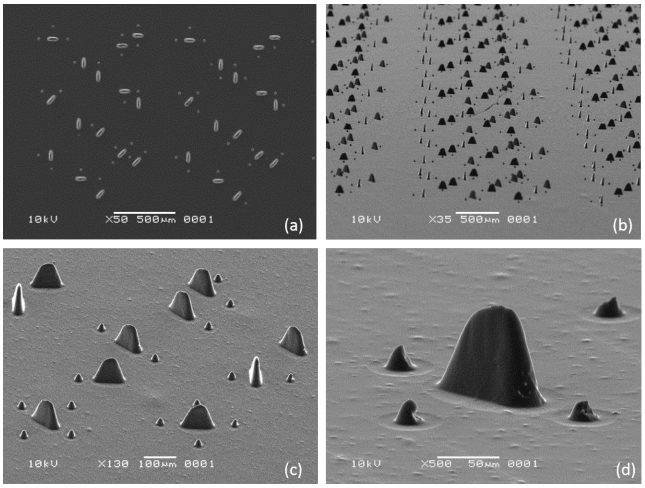

Figure 1: Microfence structures ((a) top view, (b) isometric view, (c) isometric view shown with higher magnification, (d) single microfence structure and four fiducial marks).

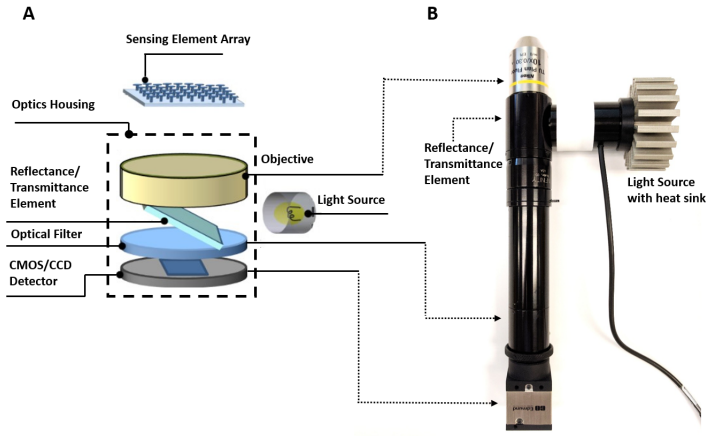

Figure 2: Schematic (A) and photograph (B) of the shear stress-sensor-prototype microscope for optical tracking.

3. Experimental Setup

To evaluate the response of the elastic microfence structures, the sensing elements were installed on a flat plate model, and subjected to controllable flow conditions in the subsonic wind-tunnel at North Carolina State University (NCSU). The details of the wind tunnel facility and flat-plate model are presented in the following subsections.

3.1. Wind-Tunnel Facility

The facility at the North Carolina State University was a closed-circuit subsonic wind tunnel with a 0.81-m high, 1.14-m wide, and 1.17-m long test section. The wind-

tunnel fan was equipped with variable-pitch blades allowing the velocity in the test section to be continuously varied up to a maximum of 40 m/s. Upstream of the test section and forward of the contraction section was a settling chamber consisting of an aluminum honeycomb screen followed by two stainless steel anti-turbulence screens. The turbulence levels have been determined to be less than 0.33%. A breather is located downstream of the test section to ventilate the tunnel to room pressure.

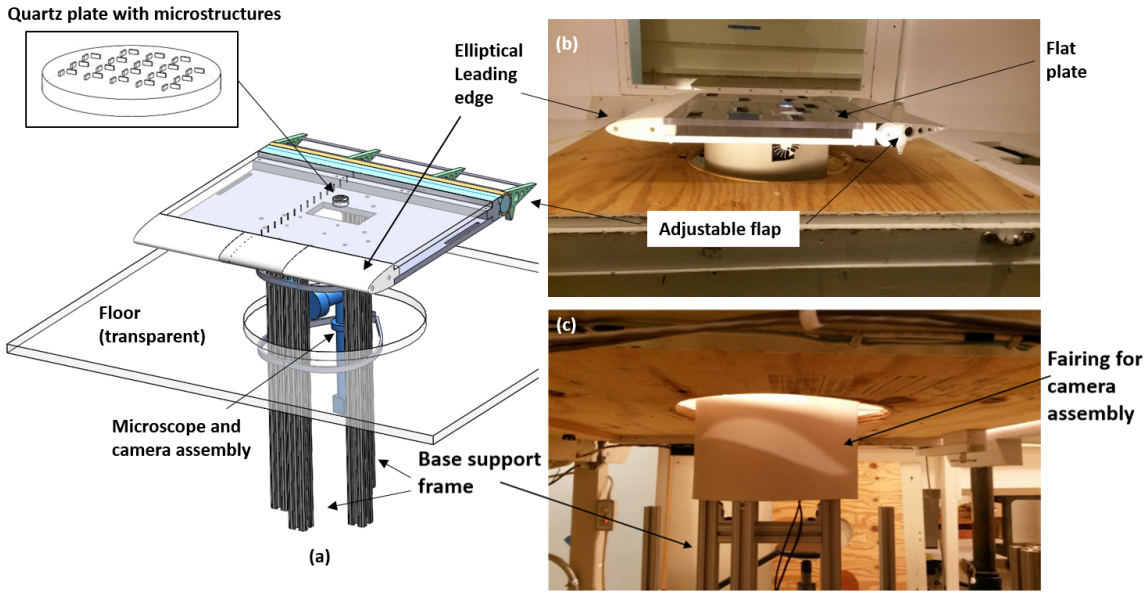

Figure 3: Flat plate model in the wind tunnel (a) drawing in which the fairing is not shown for clarity, (b) view of the model in test section, (c) view of the fairing under the test section housing the camera and microscope assembly.

3.2. Flat-Plate Model

The shear sensors were installed in the middle portion of the upper surface of a (0.66-m chord) flat-plate model with an elliptical leading edge, and a trailing edge flap that can be adjusted to control the stagnation point at the leading edge. There were surface pressure taps in the leading edge and on the upper surface of the flat plate. Figure 3 shows the flat-plate setup inside the wind-tunnel test section. The microfence sensors were installed on a small quartz disk approximately 3.175 cm in diameter, which was mounted at around 50% of the chord. A faired support structure was designed to house the camera assembly, and provide internal access for installing the prototype instrument below the quartz plate.

For one set of tests, reversed flow on the surface of the plate at the location of the microfences was achieved by using a wedge-shaped obstruction placed in front of the microfences [28, 29]. The shape and location of the wedge was selected by using surface oil-visualization to ensure that the surface flow was reversed at the location

of the microfence structures. A movable 3D-printed wedge shaped body (having a 30 degrees wedge angle, as shown in Figure 4) was fabricated for this purpose. A linear actuator was used for moving the wedge. In the default unactuated position, the wedge was located so that it was not in front of the sensor. Upon actuation, it slid in front of the microfences mounted at the mid-span location.

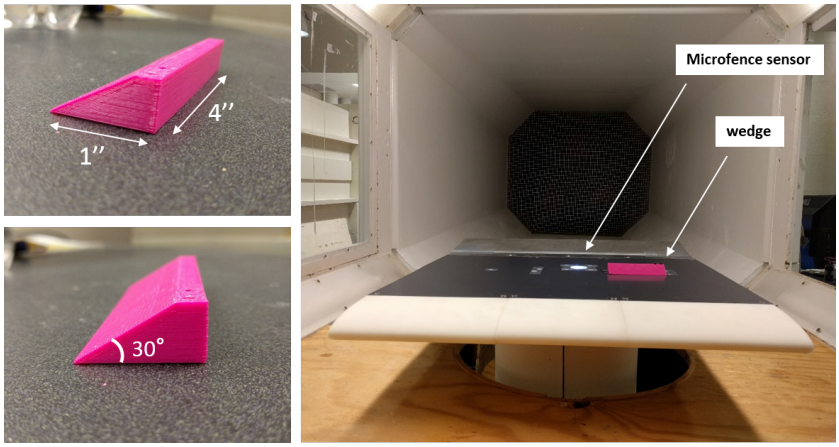

Figure 4: The 3D printed wedge with 30 degrees angle used to create flow reversal (left). A modified flat-plate setup with the wedge mechanism installed on the top surface, shown here in the unactuated position (right).

4. Data Processing

Although measures were taken in designing the current experimental setup to minimize mechanical vibrations, flow-induced vibrations were still present during the experimentation. Hence, the videos recorded during the testing required post-processing. Image-processing algorithms from MATLAB were employed for image stabilization. The images obtained from the recorded videos were first converted to grayscale format such that every pixel location has an associated intensity value. The images were adjusted to enhance the contrast between the substrate background and the microfences by linearly mapping (with a gamma correction factor of 1) the intensity values to new values such that 1% of data was saturated at low and high intensities of the original grayscale image.

Figure 5 compares a raw image (left) with the enhanced version (right). An intensity-based image registration technique generates a similarity metric between a reference image and the moved image. The similarity metric was maximized iteratively to select a transformation matrix that was used to realign the moved image with the reference. In the wind-tunnel experiments, the first frame of the video (when the freestream velocity was zero) was taken as the reference image for the test cases, and all the subsequent frames were processed and realigned based on the initial frame.

In the final post-processing step, a region of interest (of size 100 px $\times$ 100 px) was manually defined on the microstructure around the tip. The intensity values were

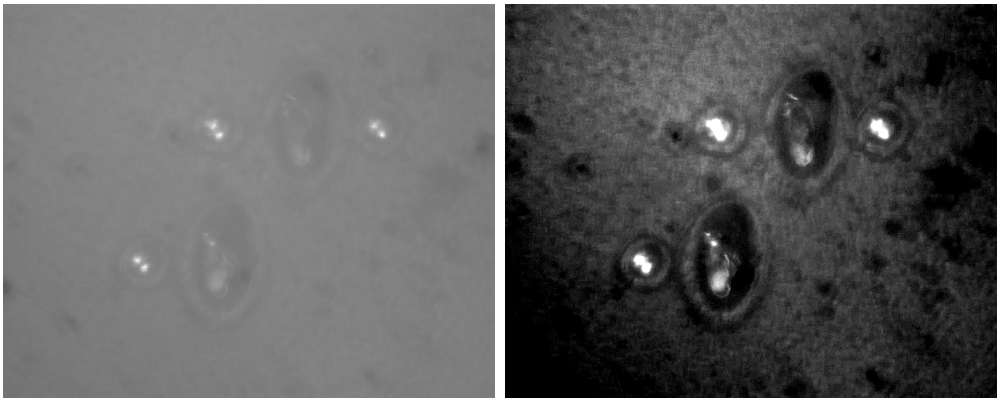

Figure 5: Raw image (left) from the video recorded in the experiments compared to the enhanced version (right) with better contrast after intensity adjustment.

investigated within the defined region to avoid the background noise from interfering with the intensity-based tracking. Within the region of interest, the minimum intensity value of the pixels at the tip of the microfence was observed in the reference image and was used to define the cutoff intensity value for all the subsequent frames. An intensity value of 150, in a grayscale range from 0 (black) to 255 (white), was used as the cutoff intensity value for the cases presented in this work. The intensity values at the microfence tip region were affected by deflection, so the centroid of pixels with intensities above a cutoff value were tracked. The movement of the tracked tip area was measured in pixels and this was converted to micrometer values based on the known length of the microfences.

5. Results

Microfence tip deflections in the flat-plate turbulent boundary layer were observed in the wind tunnel for different freestream velocities. Two different experimental setups were designed to evaluate the performance of the micro-sensors. The first test case was aimed at investigating the microfence response under the influence of different freestream velocities. The second experimental case was designed to assess the directional sensitivity of the microfences by subjecting it to local flow reversal. The results from the two test cases are presented in the following subsections.

5.1. Case 1: Effect of freestream velocity

In this test case, the microfence tip deflection was measured under four different freestream velocities: 15.2, 21.6, 24.9, and 30.5 m/s, corresponding to local Re_x of 3.4 $\times 10^5$, 4.8 $\times 10^5$, 5.9 $\times 10^5$, and 6.8 $\times 10^5$, respectively. For each Reynolds-number case, the sensor response was recorded as the velocity was steadily ramped up from zero to the required velocity. The images in Figures 6(a) and 7(a) compare the starting reference frame to frames at the steady freestream velocities of 24.9 m/s and 30.5 m/s.

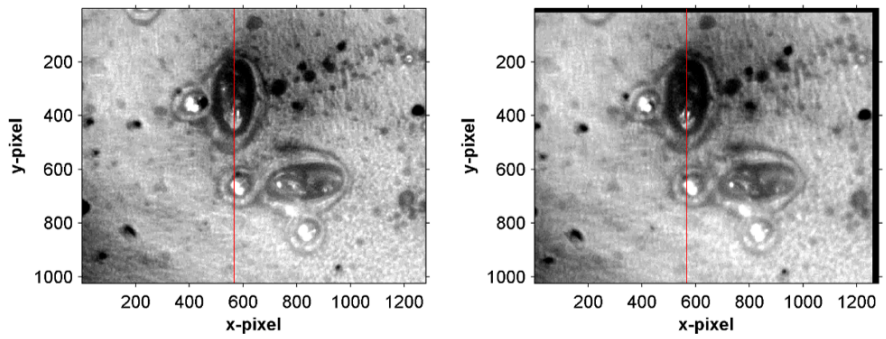

(a) Reference frame (left) and frame with deflection (right).

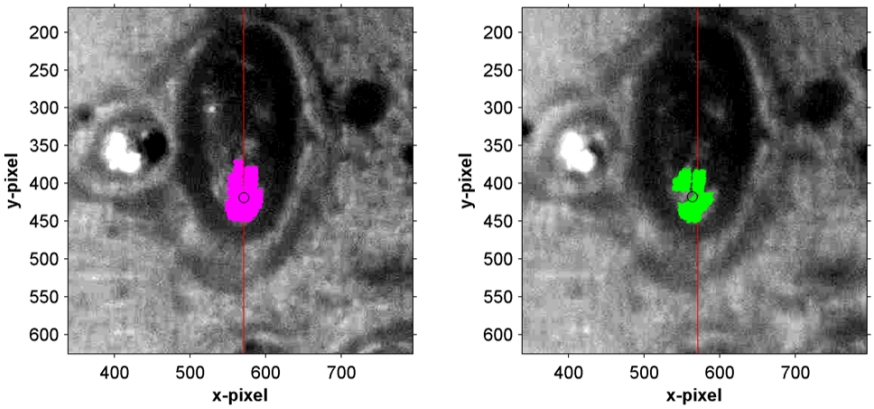

(b) Microfence tip regions marked based on intensity values for reference image (left) and deflection image (right).

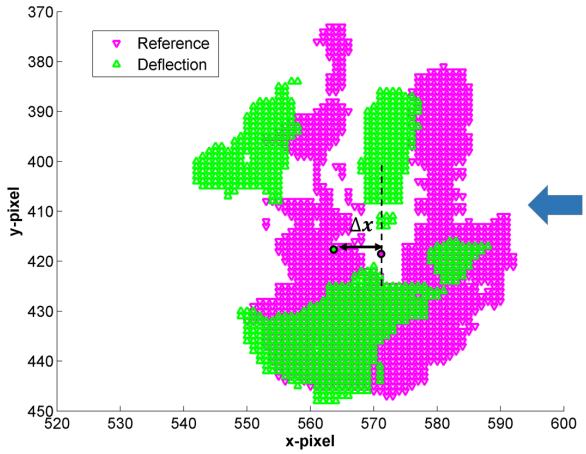

(c) Initial and final tip regions shown overlapped with circular dots indicating the respective centroids.

Figure 6: Microfence tip deflection for U_∞ of 24.9 m/s and Re_x of 5.9 $\times 10^5$, with $\Delta x =$ 7.45 px. Flow was from right to left as indicated by the blue arrow.

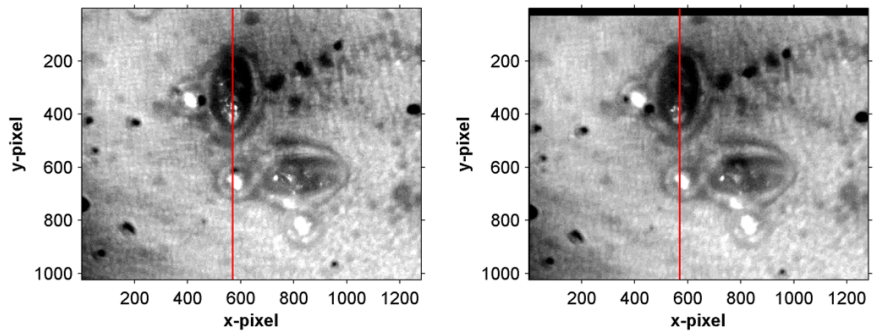

(a) Reference frame (left) and frame with deflection (right).

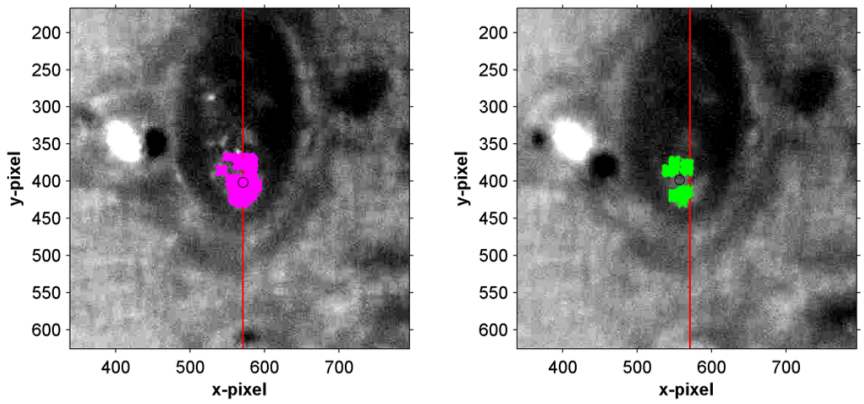

(b) Microfence tip regions marked based on intensity values for reference image (left) and deflection image (right).

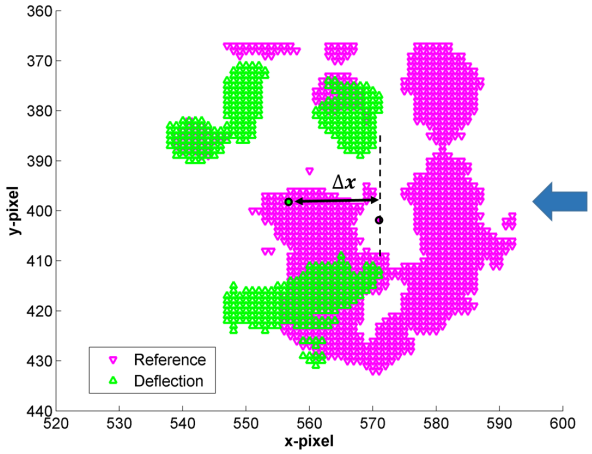

(c) Initial and final tip regions shown overlapped with circular dots indicating the respective centroids.

Figure 7: Microfence tip deflection for U_∞ of 30.5 m/s and Re_x of 6.8 $\times 10^5$, with $\Delta x =$ 14.27 px. Flow was from right to left as indicated by the blue arrow.

The microfence tip areas based on the pixel intensity levels are shown for two velocity cases in Figures 6(b) and 7(b). Since the intensity values near the tip were affected by the deflection, the tracked tip area varies, so the movement of the centroid of the tip was used to give an estimate of the pillar tip deflection, as illustrated in Figures 6(c) and 7(c). The length of the base of the microfence is approximately 93 μm and this information was used to translate the pixel deflections to micron scale. The estimated deflections for all the velocity cases are tabulated in Table 2 and plotted in Figure 8, along with the corresponding values in micrometers, μm.

Table 2: Microfence deflections observed for different freestream velocity cases.

U_∞ (m/s)	Δx (px)	$\Delta x(\mu m)$
0	0	0
15.28	2.67	1.05
21.61	4.25	1.67
26.47	7.45	2.93
30.56	14.27	5.61

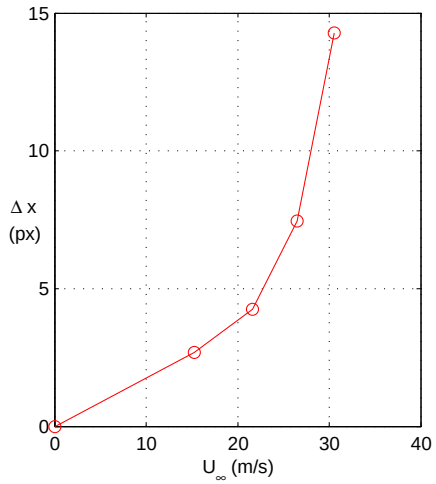

Figure 8: Variation of microfence tip deflection with freestream velocity.

5.2. Case 2: Detection of reversed flow

Figure 4 shows the flat plate inside the wind tunnel with the wedge installed on it. The test sequence with the corresponding micropillar response at reversed flow conditions is presented in Figure 9 for a U_∞ of 24.9 m/s.

The effect of reversed flow on the microfence tip deflections for two freestream velocities are presented in Figure 10. An increase in the deflection could be observed as the velocity was steadily increased from zero to the desired value. When the wedge was actuated towards the sensor (at approximately 140 seconds), a decrease in deflection

values were observed because the flow was reversed at the sensor location in the presence of the wedge. Finally, as the wedge was moved back (at approximately 185 seconds), the microfence tip again deflected in the freestream flow direction as evident from the plots in Figure 10. Although the data exhibits fluctuations due to the flow-induced vibrations, a noticeable trend can be easily detected that demonstrates the directional response of the microfence pillar. It is noted that the scatter in the deflection of the microfence pillar in the current work was much larger than that reported in [12, 15]. It is believed that the increased scatter in the current work could be reduced with improved image processing techniques that can further minimize the effects of vibration and can separate the microfence tip region from the noisy background more accurately. Creating a fixture for the camera assembly outside the wind-tunnel test section, instead of mounting the camera as a part of the same structure as the airfoil holding the sensor array, could also help in decreasing the scatter. For the purpose of detecting surface-flow reversal, the results show that the scatter does not pose a major problem.

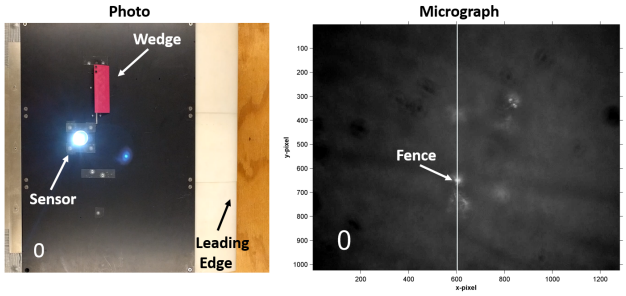

(a) State - 0 : Zero freestream velocity and wedge placed away from microfence location.

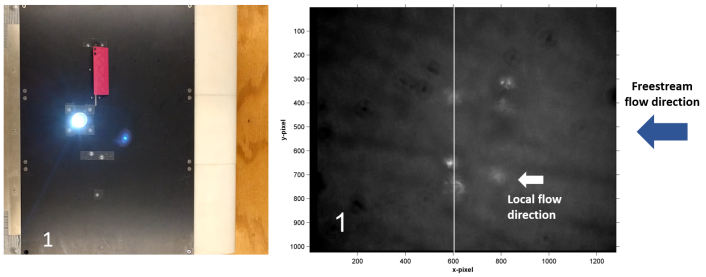

(b) State - 1 : Desired freestream velocity is attained but the wedge is still away from microfence location.

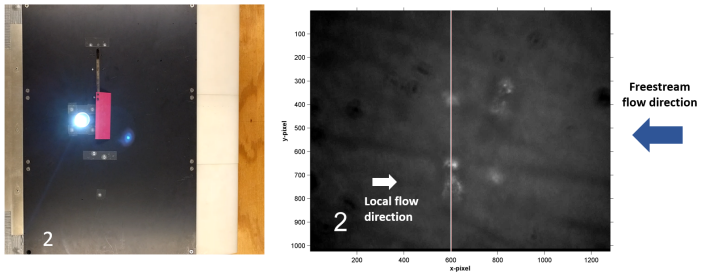

(c) State - 2 : Desired freestream velocity with wedge moved in front of the microfence location.

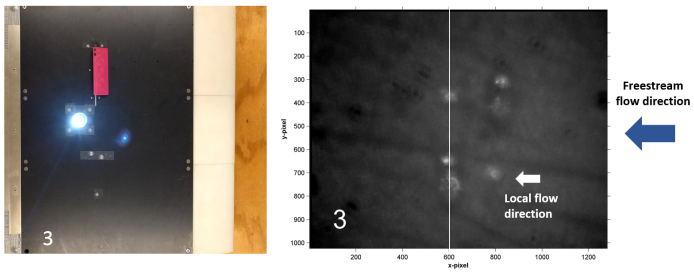

(d) State - 3 : Desired freestream velocity with wedge moved away from the microfence location.

Figure 9: Micropillar image (micrograph) with a white vertical line marking the initial reference location of the microfence tip. Top view of the flat plate (left images) shows the corresponding location of the wedge. The blue markers indicate the direction of the freesteam flow and the white arrows indicate the local flow direction observed by the microfence sensor.

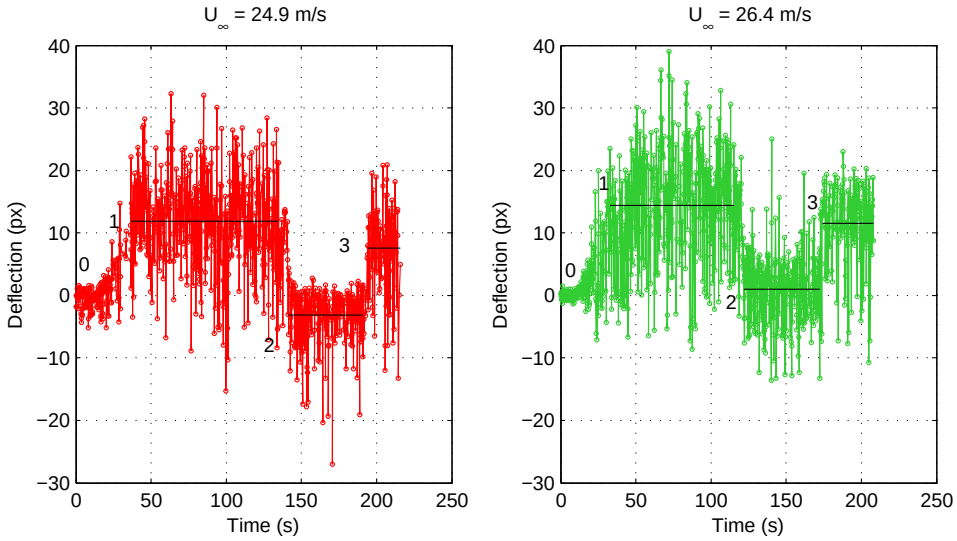

(a) $U_\infty = 24.9$ m/s. (b) $U_\infty = 26.4$ m/s.

Figure 10: The deflection (in pixels) of the microfence sensor with time as the velocity is increased and the wedge is translated towards the sensor location and then moved away.

6. Summary and conclusions

The use of microfence sensing elements for aerodynamic flow sensing was investigated in this research. Elastic surface topographies were designed to be responsive to near-wall flow behavior. The microfence structures were mounted on a flat-plate experimental setup for characterization under controllable flow conditions. The response of the sensors at different freestream velocities and directional sensitivity under reversed-flow conditions were evaluated during the wind-tunnel experiments. Image-processing algorithms were employed for image contrast improvement and for minimizing the errors induced due to vibrations in the wind tunnel. Microfence responses to flow conditions on an airfoil surface were observed at the scale of wind-tunnel investigations. It was observed that the microfence tip deflection increased with an increase in freestream flow velocity and the expected negative deflection of the microfences under reversed flow conditions were successfully measured. The image stabilization algorithm was shown to be partially successful removing vibration from the raw data.

.

[1] Susanne Sterbing-D'Angelo, Mohit Chadha, Chen Chiu, Ben Falk, Wei Xian, Janna Barcelo, John M. Zook, and Cynthia F. Moss. Bat wing sensors support flight control. *Proceedings of the National Academy of Sciences*, 108(27):11291–11296, 2011.

[2] Benjamin Dickinson, John Singler, and Belinda A Batten. The detection of unsteady flow separation with bioinspired hair-cell sensors. In *26th AIAA Aerodynamic Measurement Technology and Ground Testing Conference*, number 2008-3937. American Institute of Aeronautics and Astronautics AIAA, 2008.

[3] T Shimozawa, T Kumagai, and Y Baba. Structural scaling and functional design of the cercal wind-receptor hairs of cricket. *Journal of Comparative Physiology A*, 183(2):171–186, 1998.

[4] Graham K Taylor and Holger G Krapp. Sensory systems and flight stability: What do insects measure and why? *Advances in insect physiology*, 34:231–316, 2007.

[5] Richard E Brown and M Roger Fedde. Airflow sensors in the avian wing. *Journal of experimental biology*, 179(1):13–30, 1993.

[6] James R Usherwood, Tyson L Hedrick, and Andrew A Biewener. The aerodynamics of avian take-off from direct pressure measurements in canada geese (branta canadensis). *Journal of experimental biology*, 206(22):4051–4056, 2003.

[7] Philip L Richardson. How do albatrosses fly around the world without flapping their wings? *Progress in Oceanography*, 88(1):46–58, 2011.

[8] Anders Hedenström and L Christoffer Johansson. Bat flight: aerodynamics, kinematics and flight morphology. *The Journal of experimental biology*, 218(5):653–663, 2015.

[9] Sebastian Große and Wolfgang Schröder. The micro-pillar shear-stress sensor mps3 for turbulent flow. *Sensors*, 9(4):2222–2251, 2009.

[10] Sebastian Große and Wolfgang Schröder. Dynamic wall-shear stress measurements in turbulent pipe flow using the micro-pillar sensor mps 3. *International Journal of Heat and Fluid Flow*, 29(3):830–840, 2008.

[11] Sebastian Große, Bernardo Nottebrock, and Wolfgang Schröder. Measuring the two-dimensional, two-directional temporal wall-shear stress distribution with the micro-pillar shear-stress sensor mps3. In *48th AIAA Aerospace Sciences Meeting Including the New Horizons Forum and Aerospace Exposition*, page 495, 2010.

[12] EP Gnanamanickam and JP Sullivan. Image based sensor for distributed wall shear stress measurement. In *46th AIAA Aerospace Sciences Meeting and Exhibit*, page 270, 2008.

[13] EP Gnanamanickam and JP Sullivan. Unsteady distributed wall shear stress measurements in fluid flows. In *49th AIAA Aerospace Sciences Meeting including the New Horizons Forum and Aerospace Exposition*, page 1097, 2010.

[14] EP Gnanamanickam and JP Sullivan. Manufacture of high aspect ratio micro-pillar wall shear stress sensor arrays. *Journal of Micromechanics and Microengineering*, 22(12):125015, 2012.

[15] EP Gnanamanickam, B Nottebrock, S Große, JP Sullivan, and W Schröder. Measurement of turbulent wall shear-stress using micro-pillars. *Measurement Science and Technology*, 24(12):124002, 2013.

[16] Jonathan W Naughton and Mark Sheplak. Modern developments in shear-stress measurement. *Progress in Aerospace Sciences*, 38(6):515–570, 2002.

[17] Gregory J Ehlert, Matthew R Maschmann, and Jeffery W Baur. Electromechanical behavior of aligned carbon nanotube arrays for bio-inspired fluid flow sensors. In *SPIE Smart Structures and Materials+ Nondestructive Evaluation and Health Monitoring*, pages 79771C–79771C. International Society for Optics and Photonics, 2011.

[18] C Pozrikidis. Shear flow over cylindrical rods attached to a substrate. *Journal of Fluids and Structures*, 26(3):393–405, 2010.

[19] DM Phillips, CW Ray, BJ Hagen, W Su, JW Baur, and GW Reich. Detection of flow separation and stagnation points using artificial hair sensors. *Smart Materials and Structures*, 24(11):115026, 2015.

[20] D Roche, C Richard, L Eyraud, and C Audoly. Piezoelectric bimorph bending sensor for shear-

stress measurement in fluid flow. *Sensors and Actuators A: Physical*, 55(2):157–162, 1996.

[21] Taeyang Kim, Aditya Saini, Jinwook Kim, Ashok Gopalarathnam, Yong Zhu, Frank L Palmieri, Christopher J Wohl, and Xiaoning Jiang. A piezoelectric shear stress sensor. In *SPIE Smart Structures and Materials+ Nondestructive Evaluation and Health Monitoring*, pages 98032S–98032S. International Society for Optics and Photonics, 2016.

[22] Taeyang Kim, Aditya Saini, Jinwook Kim, Ashok Gopalarathnam, Yong Zhu, Frank L Palmieri, Christopher J Wohl, and Xiaoning Jiang. Piezoelectric floating element shear stress sensor for the wind tunnel flow measurement. *IEEE Transactions on Industrial Electronics*, 64(9):7304–7312, 2017.

[23] AMK Dagamseh, RJ Wiegerink, TSJ Lammerink, and GJM Krijnen. Towards a high-resolution flow camera using artificial hair sensor arrays for flow pattern observations. *Bioinspiration & biomimetics*, 7(4):046009, 2012.

[24] M Dijkstra, JJ Van Baar, RJ Wiegerink, TSJ Lammerink, JH De Boer, and GJM Krijnen. Artificial sensory hairs based on the flow sensitive receptor hairs of crickets. *Journal of micromechanics and microengineering*, 15(7):S132, 2005.

[25] Nannan Chen, Craig Tucker, Jonathan M Engel, Yingchen Yang, Saunvit Pandya, and Chang Liu. Design and characterization of artificial haircell sensor for flow sensing with ultrahigh velocity and angular sensitivity. *Microelectromechanical Systems, Journal of*, 16(5):999–1014, 2007.

[26] BT Dickinson, JR Singler, and BA Batten. Mathematical modeling and simulation of biologically inspired hair receptor arrays in laminar unsteady flow separation. *Journal of Fluids and Structures*, 29:1–17, 2012.

[27] Alexxandra Cisotto, Frank L Palmieri, Aditya Saini, Yi Lin, Christopher S Thurman, Jinwook Kim, Taeyang Kim, John W Connell, Yong Zhu, Ashok Gopalarathnam, et al. Shear stress sensing with elastic microfence structures. In *31st AIAA Aerodynamic Measurement Technology and Ground Testing Conference*, page 2407, 2015.

[28] W Rodi. On the simulation of turbulent flow past bluff bodies. *Journal of Wind Engineering and Industrial Aerodynamics*, 46:3–19, 1993.

[29] Arnab Kumar De and Amaresh Dalal. Numerical simulation of unconfined flow past a triangular cylinder. *International Journal for Numerical Methods in Fluids*, 52(7):801–821, 2006.